

Shape-asymmetry and flexibility in active cross-stream migration in nonuniform shear

Derek C. Gomes^{1,*} and Tapan C. Adhyapak^{1,†}

¹*Department of Physics, Indian Institute of Science Education and Research (IISER) Tirupati, Tirupati, Andhra Pradesh, 517619, India*

(Dated: February 7, 2025)

We show that the interplay of activity and broken fore-aft symmetry of shapes helps microswimmers to migrate across streamlines in nonuniform shear, emphasizing a hitherto overlooked fundamental cause of active cross-stream migration in imposed flows. Using a framework on model flagellated microswimmers in a microchannel flow, we find that besides the broken head-tail shape-symmetry, extended hydrodynamic coupling is vital for cross-stream migration, whereas flagellar flexibility significantly affects the same. Furthermore, by simplifying the problem to a basic analytical model, we are able to identify the fundamental factors affecting the observed rich *nonlinear dynamics* and predict the sorting and control of microswimmer populations inside a microchannel. Our predictions are general and apply to both *living* and *artificial* microswimmers, whereas the hydrodynamic framework developed here is necessary to probe other scenarios, such as in dense suspensions, where non-uniform shear and near-field flows become important.

Most theoretical studies on active suspensions treat the physical shape of suspended active particles as rigid and head-tail symmetric (HTS) [1–4]. Assumed as such, the dynamics of a given particle decouples from the particle’s own active flows, whereas the coupling to any external flow is centrosymmetric and non-extended [5]. While the approach is successful in deducing many experimentally validated predictions and results [6–8], asymmetric coupling to external flows and self-flow coupled dynamics of active particles promise rich physics with potential biomedical and biotechnological applications.

This paper studies the dynamics of a model microswimmer with broken head-tail and axial shape-symmetries by considering an extended coupling of the swimmer to an imposed Poiseuille flow. The model consists of a finite-sized cell body and a flagellar bundle represented by a slender rod that is capable of bending at the flagellar joint [see Fig.1]. We include finely resolved hydrodynamics which couples the flows created by the cell body to the dynamics of the flagella, and vice versa. Furthermore, the external shear flow couples to the swimmer unevenly on the cell body and along the length of the flagellar rod. Our work reveals dynamics which are strikingly different from those of rigid head-tail symmetric microswimmers in Poiseuille flows and predicts novel controls of flagellated microswimmers in microchannels.

An HTS microwimmer in Poiseuille flow is known to follow trajectories that oscillate about given streamlines, while maintaining streamline motion on the average [1, 2, 9]. In contrast, here we show that head-tail asymmetric (HTA) swimmers, for most initial conditions inside the channel, migrate towards the channel walls, whereas, swimmers with initial conditions in a small region of the phase space, bounded by an *unstable limit cycle*, migrate towards the channel center. While the extended hydrodynamic coupling to the imposed flow is a crucial factor, flagellar flexibility further help evade the center, hence avoid being flushed out by the channel flow.

Most varieties of suspended active particles have pronounced head-tail asymmetric (HTA) shapes. Notable examples are the flagellated microswimmers, such as *E. coli* and *B. subtilis*, whose use as prototypical *living* active particles is on the rise [7, 10–13]. Artificial microswimmers with flexible appendages are also a possibility given the rapid advances in the engineered active matter field [3, 14, 15]. The flagellar bundles forming the tails of these swimmers offer significant modulations to the dynamics of their cell bodies and, therefore, cannot always be ignored [CITE, e.g., Rheotaxis]. Here, we analyze the fundamental effects of the flagellar motion on the overall cell dynamics – an aspect that we find to be rich and significant yet hitherto insufficiently understood.

Microswimmer cross streaming predicted and demonstrated so far has been explained with HTS models and are attributed to the interplay of activity and various shape-independent factors such as inertial lifts [16], medium viscoelasticity [17], wall-interactions [18, 19], field alignment [9, 20], and unsteady flagellar beating [21], etc. In contrast, here we analyze the contribution of the *extended* hydrodynamic coupling on active HTA models and demonstrate the dominance of it in experimentally relevant situations [See, e.g., Fig. 2(e)]. The cross streaming we predict here for active HTA particles are significantly stronger than that observed for passive particles of bacterial dimensions [22], and results from an underlying mechanism that is strikingly different from that for other passive cross streaming systems [23]. After presenting our approach and results below, we further discuss how our findings are consistent with and enrich the insights into the observations reported in [24, 25].

Our model, shown in Fig. 1, is based on a flagellated bacterium having a rigid cell body and a flexible flagellar bundle. Capturing the finite size and HTA minimally, we model the cell body as a sphere of radius a centered at \mathbf{r}_S and approximate the flagellar bundle as a slender rod of length ℓ_f oriented along $\hat{\ell}_f$. One end of the rod

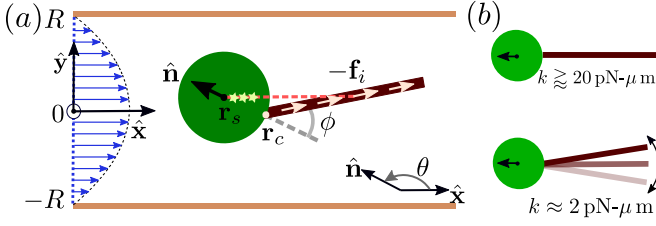


FIG. 1. (a) The model microswimmer with broken head-tail and axial symmetries in Poiseuille flow. The stars represents the distributed hydrodynamic image singularities corresponding to one of the active forces $-\mathbf{f}_i$. (b) Schematics showing the ‘rigid’ or ‘flexible’ limits of the flagella in terms of the torsional rigidity modulus k .

is attached to the cell body at $\mathbf{r}_c = \mathbf{r}_s - a\hat{\mathbf{n}}$, where $\hat{\mathbf{n}}$ is the cell’s intrinsic orientation. Flagellar bending from the swimmer’s intrinsic axis [26], is captured minimally by allowing a bend angle ϕ [Fig. 1], which is opposed by an *elastic* restoring torque $\mathbf{T}_f^{\text{el}} = -k\phi\hat{\boldsymbol{\tau}}$ on the rod, where k is a torsional rigidity modulus and $\hat{\boldsymbol{\tau}} = \hat{\boldsymbol{\ell}}_f \times \hat{\mathbf{n}} / \|\hat{\boldsymbol{\ell}}_f \times \hat{\mathbf{n}}\|$ is a unit vector normal to both $\hat{\mathbf{n}}$ and $\hat{\boldsymbol{\ell}}_f$.

As in a flagellated bacterium, we assume that the rod drives back the ambient fluid applying point forces $\{-\mathbf{f}_i^{\text{SP}}, i = 1 \text{ to } N\}$, located at uniformly distributed points along the rod. The reactionary self-propulsion force $\mathbf{F}^{\text{SP}} = \sum_i \mathbf{f}_i^{\text{SP}}$ by the fluid is transferred to the cell body to act at \mathbf{r}_c . By construction, the model runs at a given active force strength F^{SP} , hence on constant activity [6], however, due to the allowed flagellar bending it is capable of adjusting its translational and rotational self-propulsion velocities dynamically and spontaneously according to its environments (*e.g.*, in response to a crowd or imposed flows).

Equations of motion – At low Reynolds numbers [27], the swimmer’s overdamped dynamics is governed by the force and torque balance conditions:

$$\mathbf{F}_S + \mathbf{F}_f + \mathbf{F}^{\text{SP}} = 0, \quad (1)$$

$$\mathbf{T}_S + \mathbf{T}_f + \mathbf{T}^{\text{SP}} = 0, \quad (2)$$

which include all force and torque contributions by the fluid on the swimmer, the latter being evaluated about \mathbf{r}_c , for simplicity. Here, $\mathbf{F}_S = -6\pi\eta a(\mathbf{v}_S - \mathbf{v}_S^0)$ and $\mathbf{T}_S = -8\pi\eta a^3(\boldsymbol{\omega}_S - \boldsymbol{\omega}_S^0) + a(\hat{\mathbf{n}} \times \mathbf{F}_S)$, are, respectively, the viscous force and torques on the cell body, and,

$$\mathbf{F}_f = - \int_0^{\ell_f} \boldsymbol{\rho} \cdot [\mathbf{v}_f(s) - \mathbf{v}_f^0(s)] ds \quad (3)$$

$$\mathbf{T}_f = - \int_0^{\ell_f} s \hat{\boldsymbol{\ell}}_f \times \boldsymbol{\rho} \cdot [\mathbf{v}_f(s) - \mathbf{v}_f^0(s)], \quad (4)$$

are those on the flagella, as predicted by the slender rod theory [28, 29]. η is the coefficient of viscosity and $\boldsymbol{\rho} = \rho_{\parallel} \hat{\boldsymbol{\ell}}_f \hat{\boldsymbol{\ell}}_f + \rho_{\perp} (\mathbf{I} - \hat{\boldsymbol{\ell}}_f \hat{\boldsymbol{\ell}}_f)$ the resistivity (friction per unit length) tensor of the flagellar rod [30]; \mathbf{v}_S and $\boldsymbol{\omega}_S$ are respectively the translational and rotational velocities of

the cell body and $\mathbf{v}_f(s) = \mathbf{v}_S - a(\boldsymbol{\omega}_S \times \hat{\mathbf{n}}) + s[\dot{\phi}\hat{\boldsymbol{\tau}} \times \hat{\boldsymbol{\ell}}_f]$ is the flagellar velocity at the location s from \mathbf{r}_c . The velocities $\{\mathbf{v}_S^0, \boldsymbol{\omega}_S^0, \mathbf{v}_f^0(s)\}$ denote respectively, the corresponding *freely-suspended velocities* created by the *background flows* (see below) at their respective locations. In addition, Eqs. (1)-(2) have the active force \mathbf{F}^{SP} and torque $\mathbf{T}^{\text{SP}}|_{\mathbf{r}_c} = 0$ acting on the swimmer. Furthermore, the internal elastic torque \mathbf{T}_f^{el} and its reaction $\mathbf{T}_S^{\text{el}} = -\mathbf{T}_f^{\text{el}}$ on the cell body, affect the dynamics through the torque balances on the sphere and the rod, taken separately: $\mathbf{T}_S = -\mathbf{T}_S^{\text{el}} = -k\phi\hat{\boldsymbol{\tau}}$ & $\mathbf{T}_f = -\mathbf{T}_f^{\text{el}} = k\phi\hat{\boldsymbol{\tau}}$.

Finely resolved hydrodynamics – To evaluate the *freely-suspended* velocities we first note that the flow field around the swimmer: $\mathbf{u}(\mathbf{r}) = \mathbf{u}_S^{\text{mov}}(\mathbf{r}) + \mathbf{u}_f^{\text{mov}}(\mathbf{r}) + \mathbf{u}^{\text{active}}(\mathbf{r}) + \mathbf{u}^{\text{shear}}(\mathbf{r}) + \text{Img}[\mathbf{u}_f^{\text{mov}}(\mathbf{r}) + \mathbf{u}^{\text{active}}(\mathbf{r}) + \mathbf{u}^{\text{shear}}(\mathbf{r})]$. It is a superposition of the flows created by the cell body’s movements ($\mathbf{u}_S^{\text{mov}}$), flagellar movements ($\mathbf{u}_f^{\text{mov}}$), the active forces on the fluid ($\mathbf{u}^{\text{active}}$) and the imposed shear ($\mathbf{u}^{\text{shear}}$) mentioned at the beginning. The image fields (denoted by ‘Img’) of the latter three contributions, capture the *reflected* flows off the cell body’s surface accounting for the stick boundary condition. These fields are evaluated in the detail in Appendix. Given this, $\mathbf{v}_S^0 = [1 + (a^2/6)\nabla^2]\mathbf{u}_S^0(\mathbf{r}_S)$ & $\boldsymbol{\omega}_S^0 = (1/2)\nabla \times \mathbf{u}_S^0(\mathbf{r}_S)$, where $\mathbf{u}_S^0 = \mathbf{u}_f^{\text{mov}} + \mathbf{u}^{\text{active}} + \mathbf{u}^{\text{shear}}$, is the flow in the absence of the sphere, and $\mathbf{v}_f^0(s) = \mathbf{u}(s)$, considering the *slenderness* of the flagella.

Thus, the velocities $\{\mathbf{v}_S^0, \boldsymbol{\omega}_S^0, \mathbf{v}_f^0(s)\}$ depend on the flow-fields, which in turn depend on the cell body and flagellar movements. Using their expressions, Eqs. (1) and (2) can be solved self-consistently to obtain $\mathbf{v}_S, \boldsymbol{\omega}_S$ and $\boldsymbol{\Omega}_f = \dot{\phi}\hat{\boldsymbol{\tau}}$. The dynamics of the swimmer can finally be obtained from: $d\mathbf{r}_S/dt = \mathbf{v}_S, d\hat{\mathbf{n}}/dt = \boldsymbol{\omega}_S \times \hat{\mathbf{n}}$ and $d\hat{\boldsymbol{\ell}}_f/dt = \boldsymbol{\Omega}_f \times \hat{\boldsymbol{\ell}}_f$.

In the following, we take $a = 1\mu\text{m}$, $l_f = 5a$, $\eta = 8.9 \times 10^{-4} \text{ pN s } \mu\text{m}^{-2}$, $\rho_{\parallel} = XX$, $\rho_{\perp} = XX$, regarding flagellated bacteria in room-temperature water as model systems [31]. We adjust F^{SP} so that $v_S = 50\mu\text{m/s}$ [24], and use $k = 2, 5$ and $20 \text{ pN-}\mu\text{m}$, unless otherwise stated. The three chosen values of k , correspond, respectively, to a fairly flexible, intermediate and fairly rigid flagellar bundle. Fig. 2 (a) shows the flow field $\mathbf{u}(\mathbf{r})$ in the absence of any shear, for the bending angle $\phi = 45^\circ$ for two different flagellar rigidities, $k = 2 \text{ pN-}\mu\text{m}$ (flexible) and $k = 20 \text{ pN-}\mu\text{m}$ (rigid), respectively. In both cases, $\mathbf{u}(\mathbf{r})$ is asymptotically a *stresslet* field (off-aligned to $\hat{\mathbf{n}}$), as expected, however, the proximal fields are significantly altered by non-axisymmetry.

Dynamics in non-uniform shear – We now analyze the dynamics of the swimmer in the Poiseuille flow $\mathbf{u}^{\text{shear}} = v_f(1 - y^2/R^2)\hat{\mathbf{x}}$, set up between two plane walls parallel to $\hat{\mathbf{x}}$ and placed at $y = \pm R$ [Fig. 1 (a)]. Focussing on a high Péclet number dynamics across the channel width, we restrict to the swimmer’s deterministic motion in the xy plane. Furthermore, as the shear-induced alignment is

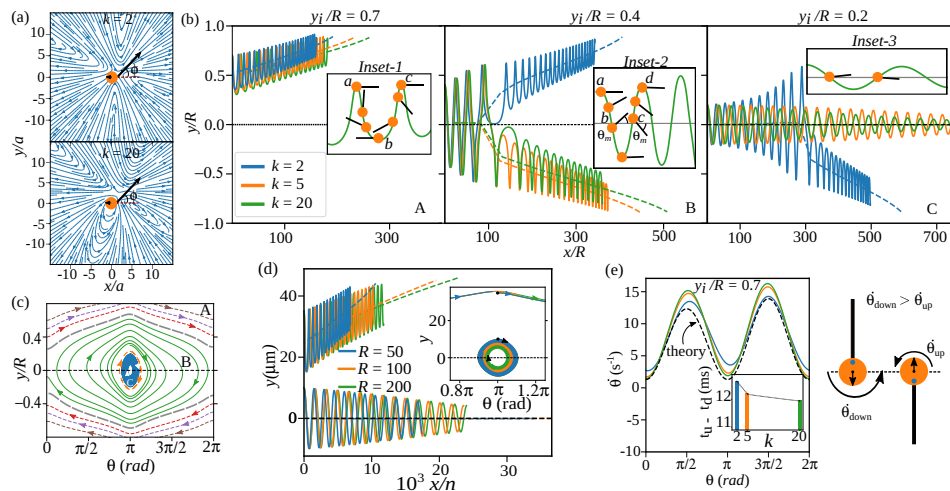


FIG. 2. (a) The intrinsic flow field of our model microswimmer for $\phi = 45^\circ$ in the flexible ($k = 2$ pN- μ m) and rigid ($k = 20$ pN- μ m) limits. (b) Trajectories of swimmers in a Poiseuille flow for varying k with initial vertical positions, y_i , chosen to capture three different classes of the observed trajectories. The flow and the trajectories run from left to right, the channel-width $R = 50 \mu\text{m}$ and $v_f = 500 \mu\text{m/s}$. *Insets*: The swimmer orientations are shown along a growing (middle panel) and decaying-amplitude (last panel) trajectory. (c) The phase space trajectories of a rigid ($k = 20$ pN- μ m) *pusher* in the y - θ plane, exhibiting an *unstable limit cycle* (orange curve). (d) Trajectories in channels of varying R when v_f/R^2 is kept constant and x is rescaled by the normalized v_f^* (see text), for $v_f/R^2 = 0.2$ and $k = 20$ pN- μ m. *Insets*: Overlapping phase space trajectories. (e) The normalized angular velocity $\dot{\theta}/\Omega_0$ Vs. θ : analytical result (dashed line) for $\phi = 0$, $y/R = 0.7$ and $k = 20$ pN- μ m; from full simulations (continuous lines) for $y_i/R = 0.7$ and k values as indicated by colors in the inset. *Inset*: $t_{\text{up}} - t_{\text{down}}$ (see text) for different k values.

‘nearly’ along the *shear-plane* [32], we assume an in-plane orientation, for simplicity. The channel parameters are set to $R = 50 \mu\text{m}$ and $v_f = 500 \mu\text{m/s}$ [24, 25], although, we checked the validity of our results for other values, too [see Figs. 2 (d) and (e)].

Our main observations are presented in Fig. 2 (b)-(d). First, we discuss the results for a *pusher* with rigid flagella ($k = 20$ pN- μ m). Fig. 2 (b) plots the trajectories traced by \mathbf{r}_S , starting from the initial upstream orientation ($\theta_i = \pi$) for various initial vertical positions (y_i). All trajectories are downstream and oscillatory. Remarkably, however, the mean paths (colored dashed lines) reveal striking cross stream migration contrasting net streamline motion of HTS swimmers [1, 2, 9]. The trajectories fall into three classes associated with distinct ranges of the initial vertical positions y_i : (A) Trajectories with large y_i gradually oscillate away from the channel axis (black dashed line) approaching the nearest wall (**Panel-1**). (B) Those with relatively smaller y_i , but above a threshold y_{max} , initially oscillate about the channel axis with *growing* amplitudes (**Panel-2**). The swimmer is thus temporarily ‘trapped’ on average to the axis until a full oscillation happens on one half of the channel, after which it ‘escapes’ towards the wall on that side. (C) Trajectories with $y < y_{\text{max}}$, however, oscillate about the channel axis with *decaying* amplitudes so that the swimmer moves downstream trapped to the channel axis for all time (**Panel-3**).

The corresponding θ -dynamics, too, show three dis-

tinct classes: In (A) $\hat{\mathbf{n}}$ rotates continuously following the fluid vorticity (counter-clockwise in the upper-half and clockwise in the lower-half of the channel). Thus, the cell tumbles, completing one full rotation approximately during one period of the spatial trajectory (*Inset-1*). In (B) and (C), on the other hand, $\hat{\mathbf{n}}$ oscillate about $\theta = \pi$, between $\theta = \pm\theta_m$, with $\theta = \pi$ marking the approximate turning points (the crests and troughs of the spatial oscillations), whereas $\theta = \pm\theta_m$ is reached near the channel axis (*Inset-2*). As in the spatial oscillations, the θ -oscillations in (B) are with growing amplitudes, $\theta_m(t)$, whereas, those in (C) are with decaying amplitudes. Accordingly, $\hat{\mathbf{n}}$ in (B) starts tumbling once the trajectory ‘escapes’ from the channel axis. In contrast, $\hat{\mathbf{n}}$ in (C) tends towards the steady state upstream orientation, $\theta = \pi$, while the swimmer gets fully trapped to the channel axis, indicating that $(y, \theta) = (0, \pi)$ is one of the dynamic *attractors* of the problem.

The effect of the full range of θ_i can be read off from the phase space diagram in the y - θ plane, plotted in Fig. 2 (c). The diagram reveals the existence of an *unstable limit cycle* (dashed orange curve) separating the growing and decaying-amplitude trajectory classes (B) and (C), respectively, discussed above. Furthermore, there is a separatrix (dashed gray curve) that separates the classes (A) and (B).

Our results show universality across channel parameters as depicted in 2 (d): Trajectories in channels of varying R are similar when v_f/R^2 is kept constant and

x is scaled by the non-dimensionalized maximum flow speed, $v_f^* = v_f / (F^{\text{SP}} / 6\pi\eta a)$. In fact, the corresponding curves perfectly overlap in the y - θ plane, indicating an invariant limit-cycle size [inset, 2 (d)].

Anomalous channel dynamics and HTA.

The oscillatory trajectories of an HTS swimmer in Poiseuille flows are attributed to the tumbling of the self-propulsion direction due to the flow induced rotations [1, 2, 9]. While the oscillations of HTA swimmers are of the same origin, the contrasting net vertical migration (along $\pm \hat{y}$), we report here, can be understood based on the asymmetric effect of the flow along the body of an HTA swimmer.

For a perfectly rigid swimmer $\hat{\ell}_f = -\hat{n}$. Therefore, considering only the dominant imposed shear flow, $\mathbf{u}^{\text{shear}}$, along the flagella background, the equations for $\mathbf{r}_S = (\dot{x}, \dot{y})$ and $\hat{\mathbf{n}} = (-\sin \theta, \cos \theta) \dot{\theta}$ yield,

$$\begin{aligned} \dot{y} &= v^{\text{SP}} \sin \theta + r_{\text{hs}} \dot{\theta} \cos \theta, \\ \dot{\theta} &= \frac{v_f}{R^2} [\alpha (1 + \beta_2 \sin^2 \theta) y + \beta_1 \sin \theta + \beta_3 \sin^3 \theta], \end{aligned} \quad (5)$$

where, the coefficients $\beta_i \rightarrow 0$ and $\alpha \rightarrow 1$, as $\ell_f \rightarrow 0$; $v^{\text{SP}} = F^{\text{SP}} / (6\pi\eta a + \rho_{\parallel} \ell_f)$ and r_{hs} is interpreted as the *shift* of the hydrodynamic center of rotation from \mathbf{r}_s [see Appendix]. Note that for an HTS swimmer, $r_{\text{hs}}, \beta_1, \beta_3 = 0$ and β_2 is the familiar Jeffery co-efficient [2]. Further, the shape-HT symmetry is purely broken by the β_1 and β_3 terms alone.

Eqs. (5) and (6) imply a y - θ dynamics that is decoupled from that of x . The resultant analytical expression for $\dot{\theta}(\theta)$ at a fixed y corresponding to the tumbling trajectories [Class-(A)], is plotted in Fig. 2 (e). The range $\theta \in [0, 2\pi]$ used here, corresponds to one spatial period seen in Panel-1 of 2 (b), where y varies during the motion. Despite this, the analytical plot captures the actual trend obtained from the simulations remarkably well. The plot indicates a relatively smaller average $\dot{\theta}$ when the swimmer faces the wall ($\theta \in [0, \pi]$) than when it faces the channel axis ($\theta \in [\pi, 2\pi]$) *i.e.*, segment $ab < bc$ in Inset-1, 2 (b). Therefore, the swimmer spends more time facing the wall and hence is driven there by its active velocity. The asymmetry in $\dot{\theta}$ is expected because of the head-tail asymmetry about \mathbf{r}_S [33], and the non-uniform shear rate that increases from the axis to the wall: when the swimmer faces the wall, its ‘tail’ faces the low shear rate region, whereas the opposite is true when it faces the channel axis [see schematic, Fig. 2 (e)]. This explains the origin of the vertical migration claimed above.

The inset in Fig. 2 (e) provides a quantitative estimate for the difference in time spent facing the centerline vs. the boundary ($t_{\text{up}} - t_{\text{down}} = \int_0^\pi d\theta / \dot{\theta} - \int_\pi^{2\pi} d\theta / \dot{\theta}$) and shows that this difference increases with greater flagellar flexibility (*i.e.*, lesser value of k), further explaining why the more flexible swimmer reaches the channel boundary faster [Fig. 2(b)].

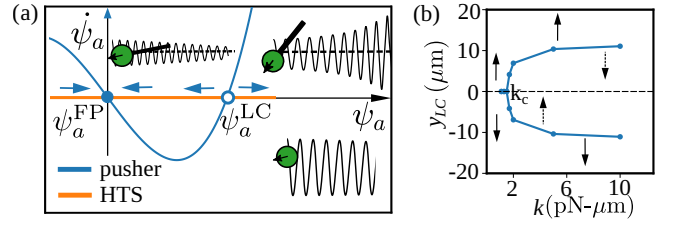


FIG. 3. (a) Schematic of $\dot{\psi}_a$ Vs. ψ_a displaying the stable (filled circle) and unstable (open circle) fixed points for a *pusher* and an HTS microswimmer. (b) Variation of the *unstable limit cycle* size in the neighborhood of $\theta = \pi$ [see, Fig. 2 (c)], as a function of flagellar flexibility.

The growing amplitude trajectories [Class-(B)] can similarly be understood. When the swimmer’s initial condition is such that it crosses $y = 0$, the vorticity direction gets reversed and hence the swimmer swings back and forth about the channel axis. For an HTS swimmer these oscillations are with constant amplitudes. Here, however, $\dot{\theta}$ has an asymmetry which flips across the channel-axis so that in either half of the channel, the swimmer spends more time while facing the wall than otherwise, implying that the segment $ab < cd$ in Inset-2, 2 (b). Besides explaining the growing amplitudes, this implies a growing θ_m , which when becomes 2π , the swimmer is fully able to tumble in the present half of the channel, marking the beginning of the ‘escaping’ and tumbling trajectory mentioned above.

Limit cycle and trapping to the channel center:

Upon eliminating y from Eq. (6), and expanding it about the only stable fixed point (FP), $(y^*, \theta^*) = (0, \pi)$, admitted by Eqs. (5) and (6), we get up to the lowest nonlinear order,

$$\ddot{\psi} = -\mu_1 (1 - \zeta \psi^2) \dot{\psi} - k_1 \psi - \mu_3 \psi \dot{\psi}^2 - k_3 \psi^3. \quad (7)$$

Here, ψ and $\dot{\psi}$ are *small deviations* from the FP-values of θ and $\dot{\theta}$, respectively, and $\mu_1, k_1 > 0$, for a *pusher*. Note that with only the first two terms on the left hand side, the equation resembles the well-known van der Pol equation (vdPE) differing only in the sign of μ_1 . Despite these differences, for small values of $\mu_1 / \sqrt{k_1} = \epsilon, \mu_3 / \zeta$ and $k_3 / \zeta k_1$, the full Eq. (7), as in vdPE, has the approximated solution $\psi(t') = \psi_a(\tau) \cos(t' + \varphi(\tau))$, with $\tau = \epsilon t'$ and $t' = \sqrt{k_1} t$.

Following the standard *Averaging Theory* [34], we obtain the time variation of the amplitude of the θ -oscillations about the FP, as $\dot{\psi}_a = -(\mu_1 \sqrt{\zeta} / 8) \psi_a (4 / \zeta - \psi_a^2)$, where the derivative is w.r.t. t . Thus, as shown in Fig. 3 (a), $\dot{\psi}_a$ has a *stable* FP, $\dot{\psi}_a^{\text{FP}} = 0$, clearly corresponding to the FP, $(y^*, \theta^*) = (0, \pi)$. The *unstable* FP, $\dot{\psi}_a^{\text{LC}}$, on the other hand implies a unique constant amplitude oscillation (*i.e.*, a closed orbit in the y - θ space), predicting the *unstable limit cycle* plotted in Fig. 2(c). Further, this also implies that oscillations

with $\psi_a < \psi_a^{\text{LC}}$ have decaying amplitude trajectories, explaining the Class-C trajectories [Panel-3, Fig. 2 (b)]. Similarly, the growing amplitude trajectories (Class-B) correspond to the amplitudes $\psi_a > \psi_a^{\text{LC}}$.

Remarkably, the solution $\psi_a(t) = 2\{\zeta - \exp(\mu t)[\zeta - 4\psi_a^{-2}(0)]\}^{-1/2}$ obtained from above, captures the qualitative rates of the amplitude growth and decay seen in Fig. 2 (b). We also find that the phase $\varphi(t)$ varies with time, unlike in vdPE, providing a first order explanation for the wavelength variations along the trajectories observed in that figure.

The framework of extended hydrodynamic coupling developed in our work is helpful to capture novel features of active particle dynamics in external flows. Imposed flows are ubiquitous in natural environments of microswimmers. Although, we consider Poiseuille flow for the simplicity and its prevalence, there is ground to expect that our basic findings are general and are valid in any non-uniform shear flows. In particular, the flows can be due to other swimmers in a suspension, in which case, our framework and results will be useful to uncover yet unknown properties of interactions and collective dynamics in suspensions, especially in the dense regimes [35].

Acknowledgments – TCA acknowledges grants CRG/2021/004759 from the Science and Engineering Research Board (India) and MoE-STARS/STARS-2/2023-0814 for financial support. DCG acknowledges PMRF, Govt. of India, for fellowship and funding. TCA and DCG express gratitude to *Indian Institute of Science Education and Research (IISER) Tirupati* for funds and facilities. Furthermore, the support and the resources provided by ‘PARAM Brahma Facility’ under the National Supercomputing Mission, Government of India at the *Indian Institute of Science Education and Research (IISER) Pune* are gratefully acknowledged.

* derekgomes@students.iisertirupati.ac.in

† Author to whom correspondence should be addressed: adhyapak@labs.iisertirupati.ac.in

- [1] A. Zöttl and H. Stark, *Phys. Rev. Lett.* **108**, 218104 (2012).
- [2] A. Zöttl and H. Stark, Periodic and quasiperiodic motion of an elongated microswimmer in poiseuille flow, *The European Physical Journal E* **36**, 1 (2013).
- [3] J. R. Howse, R. A. Jones, A. J. Ryan, T. Gough, R. Vafabakhsh, and R. Golestanian, Self-motile colloidal particles: from directed propulsion to random walk, *Physical review letters* **99**, 048102 (2007).
- [4] L. Caprini and H. Löwen, Flocking without alignment interactions in attractive active brownian particles, *Phys. Rev. Lett.* **130**, 148202 (2023).
- [5] For rigid and symmetric particles, the coupling to the external flows is through the flow vorticity and Faxén’s theorem, or its extended version [36], which simply uses derivatives evaluated at the center of the particles.
- [6] M. C. Marchetti, J.-F. Joanny, S. Ramaswamy, T. B. Liverpool, J. Prost, M. Rao, and R. A. Simha, Hydrodynamics of soft active matter, *Reviews of modern physics* **85**, 1143 (2013).
- [7] A. P. Berke, L. Turner, H. C. Berg, and E. Lauga, Hydrodynamic attraction of swimming microorganisms by surfaces, *Phys. Rev. Lett.* **101**, 038102 (2008).
- [8] I. Buttinoni, J. Bialké, F. Kümmel, H. Löwen, C. Bechinger, and T. Speck, Dynamical clustering and phase separation in suspensions of self-propelled colloidal particles, *Phys. Rev. Lett.* **110**, 238301 (2013).
- [9] X. Garcia, S. Rafaï, and P. Peyla, *Phys. Rev. Lett.* **110**, 138106 (2013).
- [10] C. Chen, S. Liu, X.-q. Shi, H. Chaté, and Y. Wu, Weak synchronization and large-scale collective oscillation in dense bacterial suspensions, *Nature* **542**, 210 (2017).
- [11] Marcos, H. C. Fu, T. R. Powers, and R. Stocker, Bacterial rheotaxis, *Proceedings of the National Academy of Sciences* **109**, 4780 (2012).
- [12] J. Dunkel, S. Heidenreich, K. Drescher, H. H. Wensink, M. Bär, and R. E. Goldstein, Fluid dynamics of bacterial turbulence, *Phys. Rev. Lett.* **110**, 228102 (2013).
- [13] H. M. López, J. Gachelin, C. Douarche, H. Auradou, and E. Clément, Turning bacteria suspensions into superfluids, *Phys. Rev. Lett.* **115**, 028301 (2015).
- [14] Z. Ye, S. Régnier, and M. Sitti, Rotating magnetic miniature swimming robots with multiple flexible flagella, *IEEE Transactions on Robotics* **30**, 3 (2014).
- [15] M. Pal, I. Fouxon, A. M. Leshansky, and A. Ghosh, Fluid flow induced by helical microswimmers in bulk and near walls, *Phys. Rev. Res.* **4**, 033069 (2022).
- [16] A. Choudhary, S. Paul, F. Rühle, and H. Stark, *Comm. Phys.* **5**, 14 (2022).
- [17] A. Choudhary and H. Stark, On the cross-streamline lift of microswimmers in viscoelastic flows, *Soft Matter* **18**, 48 (2022).
- [18] A. Choudhary, K. V. S. Chaithanya, S. Michelin, and S. Pushpavanam, *Eur Phys J E Soft Matter* **44**, 1 (2021).
- [19] A. Zöttl and H. Stark, Nonlinear dynamics of a microswimmer in poiseuille flow, *Phys. Rev. Lett.* **108**, 218104 (2012).
- [20] C. M. Buness, A. Rana, C. C. Maass, and R. Dey, Electrotaxis of self-propelling artificial swimmers in microchannels, *Phys. Rev. Lett.* **133**, 158301 (2024).
- [21] T. Omori, K. Kikuchi, M. Schmitz, M. Pavlovic, C.-H. Chuang, and T. Ishikawa, Rheotaxis and migration of an unsteady microswimmer, *Journal of Fluid Mechanics* **930**, A30 (2022).
- [22] M. Tournus, A. Kirshtein, L. V. Berlyand, and I. S. Aranson, *Journal of the Royal Society Interface* **12**, 20140904 (2015).
- [23] For example, S. Reddig and H. Stark, Cross-streamline migration of a semiflexible polymer in a pressure driven flow, *J. Chem. Phys.* **135** (2011); and G. Segre and A. Silberberg, Radial particle displacements in poiseuille flow of suspensions, *Nature* **189**, 209 (1961).
- [24] R. Rusconi, J. S. Guasto, and R. Stocker, Bacterial transport suppressed by fluid shear, *Nature physics* **10**, 212 (2014).
- [25] G. Junot, N. Figueroa-Morales, T. Darnige, A. Lindner, R. Soto, H. Auradou, and E. Clément, Swimming bacteria in poiseuille flow: The quest for active bretherton-jeffery trajectories, *Europhysics Letters* **126**, 44003 (2019).

- [26] L. Turner, R. Zhang, N. C. Darnton, and H. C. Berg, *J. Bacteriol.* **192**, 3259 (2010).
- [27] J. K. Dhont, *An introduction to dynamics of colloids* (Elsevier, 1996).
- [28] C. Pozrikidis, *Introduction to Theoretical and Computational Fluid Dynamics*, EBSCO ebook academic collection (OUP USA, 2011).
- [29] S. E. Spagnolie and E. Lauga, *J. Fluid Mech.* **700**, 105 (2012).
- [30] A. T. Chwang and T. Y.-T. Wu, Hydromechanics of low-reynolds-number flow. part 2. singularity method for stokes flows, *Journal of Fluid Mechanics* **67**, 787–815 (1975).
- [31] T. C. Adhyapak and H. Stark, Zipping and entanglement in flagellar bundle of e. coli: Role of motile cell body, *Phys. Rev. E* **92**, 052701 (2015).
- [32] The effect of out-of-plane shear alignment due to chirality (if there is any) [?], is deliberated in the discussion section in the main text.
- [33] To be precise, the HT asymmetry about the hydrodynamic center $\mathbf{r}_s + \mathbf{r}_{hs}$; however, the difference can be ignored for the present discussion due to the *slenderness* of the flagellar rod (see Appendix ??).
- [34] S. H. Strogatz, *Nonlinear dynamics and chaos: with applications to physics, biology, chemistry, and engineering* (CRC press, 2018).
- [35] D. C. Gomes and T. C. Adhyapak, in preparation.
- [36] S. Kim and S. Karilla, *Microhydrodynamics: Principles and Selected Applications* (Dover Publications, New York, 2005).